Article

Numerical Studies on the Controlled Thermocapillary Migration of a Sessile Droplet

Published as part of the Industrial & Engineering Chemistry Research virtual special issue "Multiscale Modeling and Artificial Intelligence for Multiphase Flow Science".

Jin-Xin Wang, Fei-Yu Zhang, Shi-Yu Li, Yong-Pan Cheng,* Wei-Cheng Yan,* Fan Wang, Jin-Liang Xu, and Yi Sui

ACCESS | 📊 Metrics & More | 📰 Article Recommendations

ABSTRACT: The controlled migration of droplets is of great significance in industrial applications and scientific investigation. In this study, a three-dimensional model with a level-set method is established to simulate the migration of a sessile droplet on a substrate with a temperature gradient. The moving contact line is accomplished by the line-to-plane construction method with the Navier slip boundary condition. After the model is validated with reliable theoretical results, the effect of contact angle, dynamic viscosity ratio, Marangoni number, Prandtl number, and Ohnesorge number on the droplet migration is studied. The results show that at low contact angles, the droplet migrates toward the cold region of the substrate, whereas at large contact angles, the droplet migrates toward the hot region. The opposite migration directions are due to the difference in the vortex dynamics and stagnation points induced by the thermocapillary flow. The droplet migration speed can be reduced, and the direction can be changed by increasing the viscosity ratios between outer gas and inner liquid, but it can be increased with the increasing Marangoni number, with the migration direction unchanged. The thermocapillary flow is weakened with the increasing Prandtl number, leading to the decrease in migration speed at low contact angles but the increase in migration speed at large contact angles. The viscous shear force increases with the increasing Ohnesorge number, leading to a reduction in the steady droplet migration speed. These findings can provide guidance for the controlled migration of sessile droplets.
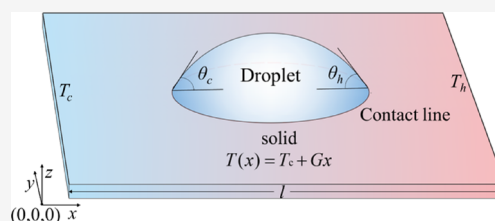
1. INTRODUCTION

The controlled migration of sessile droplet on the solid substrate is widely applied in various scientific and industrial fields, such as spray cooling,[1] 3D printing,[2] pesticide spraying,[3] and microfluidic devices.[4] The controlled migration of sessile droplet can be achieved through gravity,[5] magnetic force,[6] electric force, etc.[7] Besides the external forces, the thermocapillary force may be utilized for droplet manipulation, which is caused by the nonuniform interfacial tension force due to the temperature gradient.[8,9] For example, when a sessile droplet is deposited on a nonuniformly heated substrate, the nonuniform temperature distribution can cause the tangential thermocapillary force along the interface, forming the Marangoni flow and driving the droplet migration along the substrate.[10−13]

It is well-known that the migration of suspended droplet under the temperature gradient is toward the hot region; it was previously believed that a sessile droplet on a nonuniformly heated substrate would move toward the cold region.[9,14] Bouasse[15,16] observed the droplet migration toward the cold region of a nonuniformly heated wire. Through the lubrication theory, Ford and Nadim[17] analyzed the thermocapillary migration of droplet at low contact angles and found that the

sessile droplet moved toward the cold region of the solid substrate. Ford and Nadim[17] and Brochard[18] calculated the droplet migration speed by equating the viscous shear force on the solid substrate with the mechanical force due to the unbalanced interfacial surface tension at the contact line. The accuracy of this model was further validated through several experiments on sessile droplet migration under thermocapillary force.[19,20]

However, the lubrication theory is not applicable for droplet migration at large contact angles.[21] The direction of the driving force due to the imbalanced interfacial tension at the three-phase contact line depends on the contact angle.[22] Sui[21] found that the sessile droplet was stationary at the contact angle around 100°, and with increasing contact angle, the droplet started to move toward the hot region, in contrast to the direction at low contact

angles, and the large viscosity of external fluid could also change the droplet migration direction. Furthermore, through an experimental study, Pradhan and Panigrahi[23] found that the droplet size could also change the migration direction on a nonuniformly heated substrate. For a large droplet, the migration direction was unidirectional from the cold region to the hot region. Fath and Bothe[24] found that the migration direction was different with the classical lubrication theory, and they classified the driving force as pressure, viscous stress at the free interface, shear stress at the wall, and mechanical force at the contact line. They found that the tangential stress induced solely by temperature-dependent surface tension led to the droplet moving toward the cold region and the normal stress led to the moving toward the hot region.

Besides the droplet migration direction, the migration speed is also of great significance for controlled motion of droplets. Yin et al.[25] investigated the thermocapillary migration of a sessile droplet under a large Marangoni number. The migration process was classified into five stages: overshoot, first acceleration, plateau, second acceleration, and final steady migration. It was indicated that the increasing Marangoni number resulted in a large migration distance before the droplet attained a stable migration speed. Nguyen et al.[26] found that a large temperature gradient could lead to high stable migration speed and shorten the time to reach the stable speed. Similar results were found by Balasubramaniam et al.,[27] who found that under reduced gravity droplet, the migration speed increased linearly with the temperature gradient due to strong thermal convection. Zhao et al.[28] analyzed the migration of sessile binary droplets and found that the droplet migration speed was proportional to the droplet diameter. In addition, Tseng et al.[29] found that the contact angle and the flow field have great influence on the droplet migration speed. Wu[30] found that the droplet was deformed by reducing the droplet migration speed. Xie et al.[31] experimentally studied the thermocapillary migration of the droplet and found that the migration speed was lower than the value from the lubrication theory.

Through the aforementioned literature review, it is known that the droplet migration under thermocapillary force is affected by various factors, including droplet size, temperature gradient, physical property of the droplet, and surrounding gas. However, previous studies have primarily focused on the parametric studies on droplet migration and it is not clear how the migration speed and direction depend on those parameters. Furthermore, the two-dimensional model is mainly adopted in previous numerical simulations, which cannot reflect the three-dimensional characteristics of a real droplet. In this study, a three-dimensional numerical model with a level-set method is built up to track the dynamics of a droplet and the implementation of a contact angle adjacent to the substrate is introduced in detail. The dynamics of a sessile droplet is numerically investigated under a large range of contact angles, dynamic viscosity ratios, temperature gradients, viscosities, etc. Additionally, detailed analyses of the flow field and temperature field are conducted to elucidate the influence of the key parameters on sessile droplet migration. These findings have significant implications for the controlled manipulation of thermocapillary migration processes.

2. PHYSICAL MODEL AND NUMERICAL FORMULATION

Figure 1 illustrates the schematic diagram of the migration of a sessile droplet on a horizontally oriented substrate with a
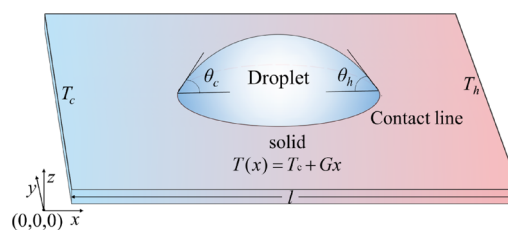
Figure 1. Schematic diagram of droplet migration on substrate with a temperature gradient due to thermocapillary force.

constant temperature gradient. The droplet is of the shape of a spherical cap under thermocapillary force. The constant temperature gradient is $G = \frac{T_h - T_c}{l}$, and the local temperature distribution is $T(x) = T_c + Gx$. The initial temperature of the droplet is $T_0 = \frac{T_h + T_c}{2}$, and the heat transfer between the droplet and substrate results in the temperature variation along the droplet surface, giving rise to the tangential thermocapillary force to drive the droplet migration. The dependence of surface tension on the temperature can be described as $\sigma(T) = \sigma_0 - \sigma_T(T - T_0)$, where σ_0 is the surface tension at reference temperature T_0 and σ_T is the surface tension variation rate over temperature.[21,32]

The imbalanced surface tension near the contact line can cause the mechanical force $F_{cl} = \sigma_h \cos\theta - \sigma_c \cos\theta$, where σ_h is the surface tension near the contact line at the hot region and σ_c is the surface tension near the contact line at the cold region. The mechanical force is determined by the temperature gradient and contact angle, and its direction can be changed by the contact angle. Upon droplet migration, a viscous shear force is generated between the droplet and substrate. When the thermocapillary force and mechanical force are in equilibrium with the viscous shear force, the droplet attains a steady migration speed. Ford and Nadim[17] developed a theoretical model to predict the droplet migration speed by equating the mechanical force and the thermocapillary force with the viscous shear force. Their model serves as a basis for validating the model in our study.

The migration of the droplet is induced by the thermocapillary force; the characteristic velocity is the capillary-inertial velocity.

$$u_0 = \sqrt{\frac{\sigma_0}{\rho_1 r_0}} \tag{1}$$

Here, σ_0, ρ_1, and r_0 are the surface tension, droplet density, and radius, respectively.

The nondimensional governing equations for the droplet migration are shown as follows:[33,34]

The continuity equation:

$$\nabla \cdot \vec{u} = 0 \tag{2}$$

The momentum equation

$$\frac{\partial \vec{u}}{\partial t} + \vec{u} \times \nabla \vec{u} = -\frac{1}{\rho^*}\nabla p + \frac{1}{\rho^* Re}\nabla \cdot [\mu^*(\nabla \vec{u} + \nabla \vec{u}^T)]$$
$$+ \frac{1 - Ma \times T}{\rho^* Re \times Ca}\kappa \vec{n}\delta(\varphi)$$
$$- \frac{Ma}{\rho^* ReCa}\nabla_S T\delta(\varphi) \tag{3}$$

The last two source terms represent the normal and tangential components of surface tension, respectively. The Reynolds number is defined as $Re = \frac{\rho_1 u_0 r_0}{\mu_1}$, the Capillary number is $Ca = \frac{\mu_1 u_0}{\sigma_0}$, and the Marangoni number is $Ma = \frac{\sigma_T r_0 \nabla T}{\sigma 0}$. The curvature is calculated as $\kappa = \nabla \times \frac{\nabla \varphi}{|\nabla \varphi|}$, and the normal vector is $\vec{n} = \frac{\nabla \varphi}{|\nabla \varphi|}$.

The energy equation

$$\frac{\partial T}{\partial t} + \vec{u} \times \nabla T = \frac{Oh}{\rho^* C_p^* Pr} \nabla \times (\lambda^* \nabla T) \tag{4}$$

The Ohnesorge number is defined as $Oh = \frac{\mu_1}{\sqrt{\rho_1 \sigma_0 r_0}}$, and the Prandtl number is $Pr = \frac{\mu_1 C_{p,1}}{\lambda_1}$.

The evolution of the droplet surface is tracked by the level-set method, the convection equation is

$$\frac{\partial \varphi}{\partial t} + \vec{u} \times \nabla \varphi = 0 \tag{5}$$

The nondimensional physical properties of dynamic viscosity μ^*, density ρ^*, specific heat C_p^*, and thermal conductivity λ^* in eq 2 and eq 4 are calculated as follows:

$$\mu^* = H(\varphi) + (1 - H(\varphi))R_v \tag{6-a}$$

$$\rho^* = H(\varphi) + (1 - H(\varphi))R_d \tag{6-b}$$

$$C_p^* = H(\varphi) + (1 - H(\varphi))R_{Cp} \tag{6-c}$$

$$\lambda^* = H(\varphi) + (1 - H(\varphi))R_c \tag{6-d}$$

The ratios of viscosity R_v, density R_d, thermal conductivity R_d, and specific heat R_{Cp} are defined as follows: $R_v = \mu_g/\mu_l$, $R_d = \rho_g/\rho_l$, $R_{cp} = C_{p,g}/C_{p,l}$, and $R_c = \lambda_g/\lambda_l$. The subscripts l and g represent the liquid and gas, respectively.

The Heaviside function is defined as

$$H(\varphi) = \begin{cases} 0, & \varphi < -\xi \\ \frac{1}{2}[1 + \varphi/\xi + \sin(\pi\varphi/\xi)/\pi], & |\varphi| \leq -\xi \\ 1, & \varphi > -\xi \end{cases} \tag{7}$$

where $\xi = 1.5\,dx$ and $\nabla H(\varphi)$ is Dirac delta function $\delta(\varphi)$ in eq 2.

In this study, the finite volume method is used to discretize the governing equations. A marker-and-cell mesh is used to overcome the checkerboard pressure field. The coupled momentum and continuity equations are solved by the standard projection method. The diffusion term and advection term are discretized with the second-order Crank−Nicolson and Adams−Bashforth schemes, respectively. The level-set advection equation is solved by the fifth-order weighted essentially nonoscillatory (WENO) scheme.[34,35] After sensitivity checking, the nondimensional computational domain is selected as $10 \times 4 \times 2$ with the grid size $201 \times 81 \times 41$ and the time step 1×10^{-4}. The default parameter settings are as follows for the reference case $Oh = 0.1$, $Ma = 0.1$, $Pr = 1$, and the ratios of gas property to liquid property are $R_d = R_v = R_{cp} = 0.1$, $R_c = 0.01$, and the contact angle is $\theta_c = \theta_h = 60°$.

3. 3D IMPLEMENTATION OF CONTACT ANGLES

It is challenging to incorporate the moving contact lines in constructing a three-dimensional droplet dynamics model.[36−38] In this study, the Navier slip boundary condition is adopted at the substrate, and the constant contact angle is implemented at the distance of half grid size from the solid boundary and adjusted in the "reinitialization" step.[39] The detailed procedure is as follows:

Step 1: Determine the Line I position of Plane I at the plane $z = 0.5\Delta z$.

In Figure 2a, Plane I is the tangential plane at which the droplet surface intersects with the substrate during surface
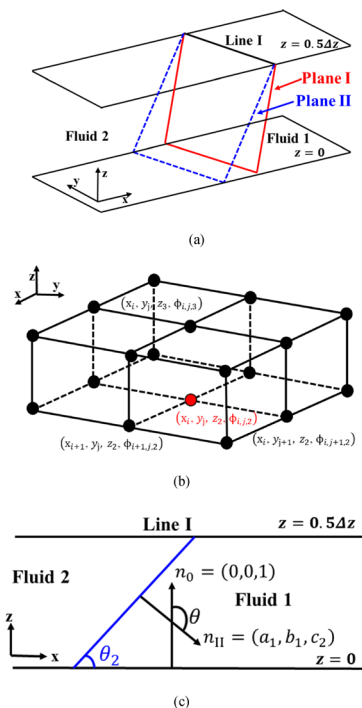
Figure 2. Schematic diagram of the implementation of moving contact line. (a) Illustration of different planes $z = 0$ and $z = 0.5\Delta z$. (b) Sketch of data set distribution. (c) Illustration of the unit normal of Plane II and plane $z = 0$.

tracking and Line I is the intersection line between the interface and the plane $z = 0.5\Delta z$. In order to locate Line I, the mathematical description of the interface needs to be obtained first. The interface is approximated by a plane as

$$\text{Plane I} \quad a_1 x + b_1 y + c_1 z + d_1 = 0 \tag{8}$$

Thus, Line I is obtained as

$$\text{Line I} \quad a_1 x + b_1 y + 0.5 c_1 \Delta z + d_1 = 0 \tag{9}$$

The signed distance $D_{i,j,k}$ from the center of a cell (i, j, k) to Plane I is calculated as

$$D_{i,j,k} = \frac{a_1 x_i + b_1 y_i + c_1 z_k + d_1}{\sqrt{a_1^2 + b_1^2 + c_1^2}} \tag{10}$$

where (x_i, y_j, z_k) is the coordinates of the cell center. The actual value of the signed distance from simulation is $\varphi_{i,j,k}$.

As shown in Figure 2b, eq 10 satisfies the condition that it is the best fit to the data set $(x_i, y_j, z_k, \varphi_{i,j,k})$ around cell $(i, j, 2)$, where cell $(i, j, 2)$ is a cell close to the interface within the first

layer of cells adjacent to the wall. In practice, the criteria $|\varphi_{i,j,k}| < 3\Delta x$ is adopted to select cell $(i,j,2)$. The least-squares algorithm is applied to construct Plane I, and the data from cell $(i,j,2)$ (red dot in Figure 2b) and its adjacent 17 cells (black dots in Figure 2b) in all three directions above the solid boundary are incorporated. The optimum in eq 11 can be found when the sum of the squared residual gets its minimum value. Here, the residual is calculated as

$$S(a_1, b_1, c_1, d_1) = \sum_{i=i-1}^{i+1} \sum_{j=j-1}^{j+1} \sum_{k=k-1}^{k+1} (\varphi_{i,j,k} - D_{i,j,k})^2 \quad (11)$$

Step 2: Update the interface Plane II was updated with the prescribed contact angle θ.

Once Line I is achieved, the new interface Plane II can be built up in accordance with the contact angle θ. As Line I is contained in Plane II, Plane II can be written as

Plane II $a_1 x + b_1 y + c_2 z + d_2 = 0 \quad (12)$

with

$$0.5c_2\Delta z + d_2 = 0.5c_1\Delta z + d_1 \quad (13)$$

It should be noted that the unit normal $\mathbf{n_{II}}$ of the interface points from $\varphi < 0$ (gas phase) to $\varphi > 0$ (liquid phase), and the unit normal of the $z = 0$ plane is taken as $\mathbf{n_0}$ pointing to the liquid, as seen in Figure 2c. The angle between $\mathbf{n_{II}}$ and $\mathbf{n_0}$ is $\theta = \pi - \theta_2$.

Since

$$\cos\theta = \frac{\mathbf{n_{II}} \cdot \mathbf{n_0}}{\|\mathbf{n_{II}}\|\|\mathbf{n_0}\|} = \frac{c_2^2}{\sqrt{a_1^2 + b_1^2 + c_2^2}} \quad (14)$$

θ_2 is calculated as

$$\cos\theta_2 = \cos(\pi - \theta) = \frac{-c_2}{\sqrt{a_1^2 + b_1^2 + c_2^2}} \quad (15)$$

so

$$c_2 = \frac{\sqrt{a_1^2 + b_1^2}}{\tan\theta} \quad (16)$$

and

$$d_2 = d_1 + 0.5\Delta z(c_1 - c_2) \quad (17)$$

Step 3: Update the level-set function

In the region near the contact line ($|\varphi_{i,j,2}| < 3\Delta x$), the level-set function at the ghost cell $\varphi_{i,j,1}$ is updated by calculating the signed distance to Plane II.

$$\varphi_{i,j,1} = \frac{a_1 x_i + b_1 y_j + c_2 z_1 + d_2}{\sqrt{a_1^2 + b_1^2 + c_2^2}} \quad (18)$$

In the rest of the region without contact lines, the level-set function in the ghost cell is extrapolated from the adjacent cells above the solid boundary.

$$\varphi_{i,j,1} = 2\varphi_{i,j,2} - \varphi_{i,j,3} \quad (19)$$

With the above procedure, the accurate representation of moving contact lines within the three-dimensional droplet dynamics model can be achieved.

4. RESULTS AND DISCUSSION

4.1. Numerical Validation. Figure 3 shows the evolution of the droplet migration speed at $\theta = 30°$ under various Marangoni
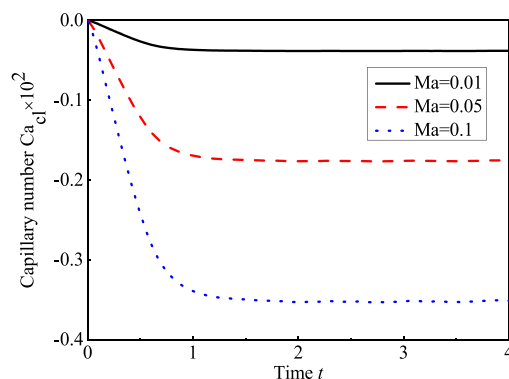
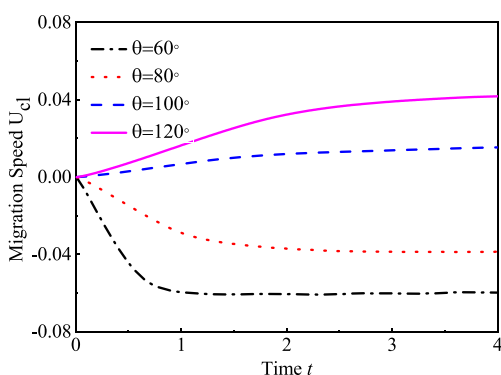**Figure 3.** Temporal evolution of the droplet migration speed under different Marangoni numbers.

numbers at the default parameters. The accuracy of the model is evaluated with the steady capillary number $Ca_{cl} = \frac{\mu_1 U_{cl}}{\sigma_0}$, which is defined with the droplet migration speed.[21] It is evident that the droplet undergoes initial acceleration before rapidly attaining a constant migration speed. A negative value of Ca_{cl} indicates that the droplet moves toward the cold region. To validate the numerical model, the capillary numbers are compared with the predicted results from the theoretical model,[17] which is based on the two-dimensional droplet shape. The steady migration speed of the droplet is predicted by equating the mechanical force and the thermocapillary force with the viscous shear force on the substrate. Figure 4 shows the satisfactory agreement between the
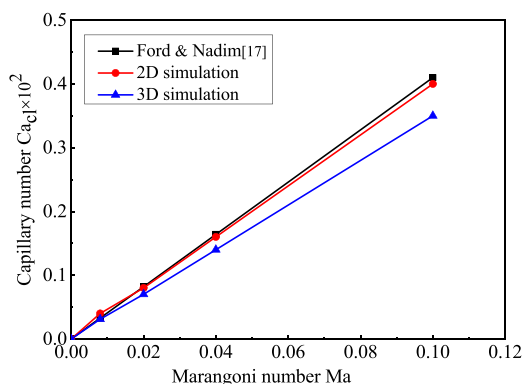
Figure 4. Comparison of 2D and 3D steady droplet migration speeds with theoretical predictions under different Marangoni numbers.

theoretical values and the 2D simulation results, but 3D simulation results are relatively lower, especially at a large Marangoni number. Because at a large Marangoni number, the strong thermocapillary flow occurs inside the droplet, the lubrication theory is no longer applicable. The comparison also shows that it is essential to adopt a 3D numerical model with moving contact lines to accurately predict the real droplet migration speed.

4.2. The Effect of Contact Angles. Figure 5 shows the temporal evolution of droplet migration speed U_{cl} under different contact angles. The droplet dynamics is characterized by initial acceleration and following rapid attainment of steady migration speed. However, the migration direction may vary, depending on the contact angle, i.e., at a large contact angle, the migration speed is positive, indicating the droplet migrates

Figure 5. Temporal evolution of the droplet migration speed under different contact angles.

toward the hot region, while at a low contact angle, the droplet migrates toward the cold region.

In order to further investigate the effect of contact angle on the droplet dynamics, the droplet migration speed is shown with the contact angle ranging from 30 to 130° under various Marangoni numbers, as shown in Figure 6. It is shown that at $\theta \leq$
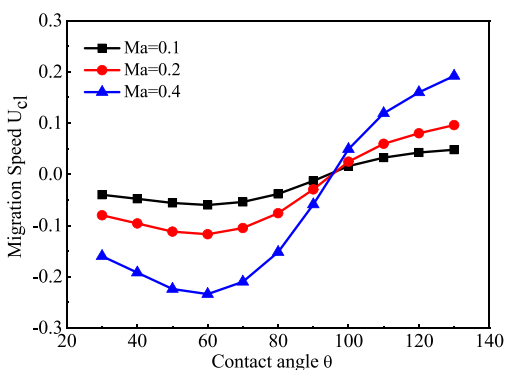
Figure 6. Effect of the contact angle on the droplet migration speed under different Marangoni numbers.

60°, the migration speed of the droplet increases as the contact angle increases, reaching its maximum at $\theta = 60°$. However, as the contact angle continues to increase beyond 60° and approaches 90°, the droplet migration speed decreases. Furthermore, at $\theta \leq 90°$, the droplet migration speed is negative, indicating that the droplet moves toward the cold region. Conversely, at $\theta \geq 100°$, the droplet migration speed becomes positive and increases with the contact angle, suggesting that the droplet migrates toward hot region.

To further study the influence of flow patterns on droplet migration under different contact angles, Figure 7 shows the steady flow patterns and temperature fields in the droplet along the $x-z$ meridian surface. At $\theta = 30°$ in Figure 7a, the flow is predominantly toward the cold region, consequently resulting in droplet migration toward the cold region. At $\theta = 60°$ in Figure 7b, a vortex is formed near the bottom of the substrate within the droplet, which is accompanied by two stagnation points. Since the stagnation points are inside the droplet, the droplet migrates toward the cold region. When the contact angle increases to 120° in Figure 7c, the vortex develops outside the droplet while the stagnation points are located outside; this prompts droplet migration toward the hot region. Interestingly, as the contact angle increases, a vortex forms and expands within the droplet until the separation points align with the contact lines. At this
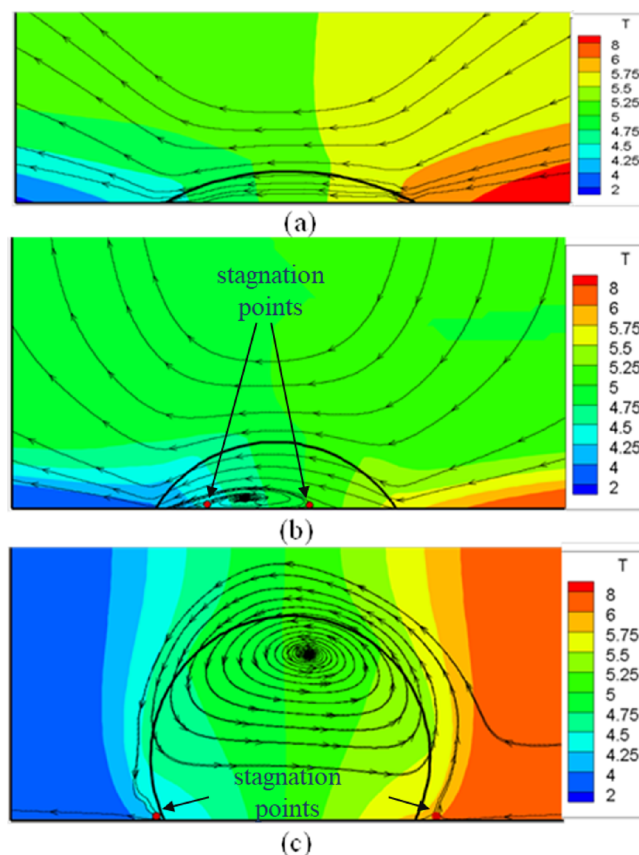

Figure 7. Flow patterns and temperature fields on the $x-z$ meridian surface of droplet at contact angle (a) $\theta = 30°$, (b) $\theta = 60°$, and (c) $\theta = 120°$.

point, the droplet remains motionless on the substrate. When the separation points are located outside the droplet, indicating the vortex is larger than the droplet region, droplet migration occurs toward the hot region.

4.3. The Effect of Dynamic Viscosity Ratios. The influence of dynamic viscosity ratios on droplet migration speed is studied at contact angles of 60 and 120°, as shown in Figure 8. It is observed that the magnitude of the droplet migration speed decreases as the dynamic viscosity ratio increases, because the viscous shear resistance surrounding the droplet is increased. The direction of migration remains unchanged at both contact angles of 60° and 120°.

In order to investigate the effect of flow patterns on droplet migration under various dynamic viscosity ratios, Figure 9 shows the steady flow patterns and temperature fields along the $x-z$ meridian surface at $\theta = 60°$. At different dynamic viscosity ratios, a single thermocapillary vortex forms within the droplet, with the separation points inside the droplet. However, with the increasing dynamic viscosity ratio, the separation points gradually shift toward outside of the droplet; the large vortex may reduce the horizontal driving force and leads to decrease in droplet migration speed.

With the increasing dynamic viscosity ratio, the vortex grows larger; however, the stagnation points still remain within the droplet. The question arises as to whether the dynamic viscosity ratio can alter the direction of droplet migration. To gain further insight into the effect of dynamic viscosity ratio and contact angle on the droplet migration direction, a phase diagram is built up to show the droplet migration direction, as illustrated in

(a)

(b)
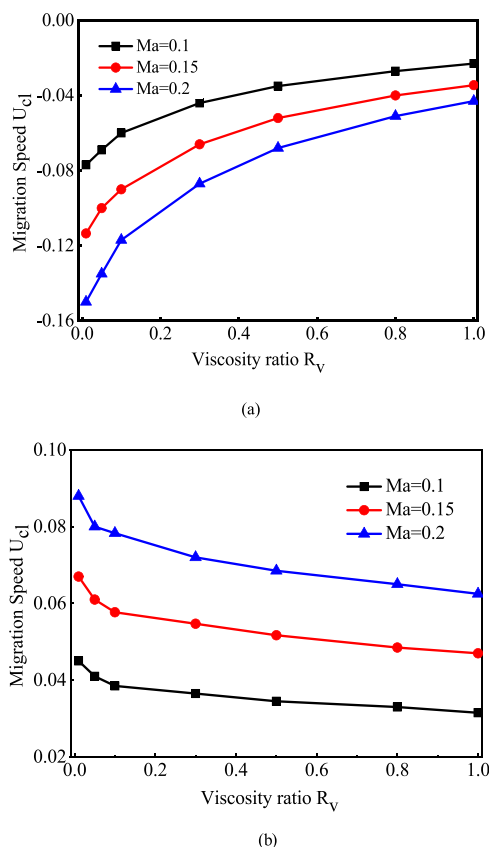
**Figure 8.** Effect of dynamic viscosity ratios on droplet migration speed at (a) $\theta = 60°$, (b) $\theta = 120°$.

Figure 10. It shows that the dynamic viscosity ratio can indeed affect the direction of the droplet migration. Generally, the droplet migrates toward the cold region at $\theta < 70°$ and toward the hot region at $\theta > 110°$. As the contact angles are between 80 and 100°, the droplet migration direction can be changed due to variations in the dynamic viscosity ratio. A high viscosity ratio facilitates the direction transition from the cold region to the hot region at low contact angles.

4.4. The Effects of Marangoni, Prandtl, and Ohnesorge Numbers. The temperature fields are affected by the Marangoni number, Prandtl number, and Ohnesorge number, which can affect the droplet migration dynamics. Figure 11 shows the droplet migration speed under different Marangoni numbers. It is observed that the droplet migration speed shows a linear increase with the Marangoni number. Regardless of the Marangoni number, droplets all migrate toward the cold region at $\theta = 60°$ and $\theta = 80°$, but at $\theta = 100°$ and $\theta = 120°$, droplets all migrate toward the hot region. These findings suggest that the Marangoni number does not affect the droplet migration direction, because with the increasing Marangoni number, the mechanical force is enhanced on the droplet, but its direction remains unaltered.

The influence of the Prandtl number on the droplet migration speed under different contact angles is shown in Figure 12. It is found that the Prandtl number exhibits different effects on the droplet migration speed depending on the contact angle. At a contact angle $\theta = 60°$, the Prandtl number has minimal impact on the steady migration speed when it is below 10. However, as the Prandtl number exceeds 10, the droplet migration speed is reduced while at contact angle $\theta = 120°$, the droplet migration speed increases with increasing Prandtl number. This can be
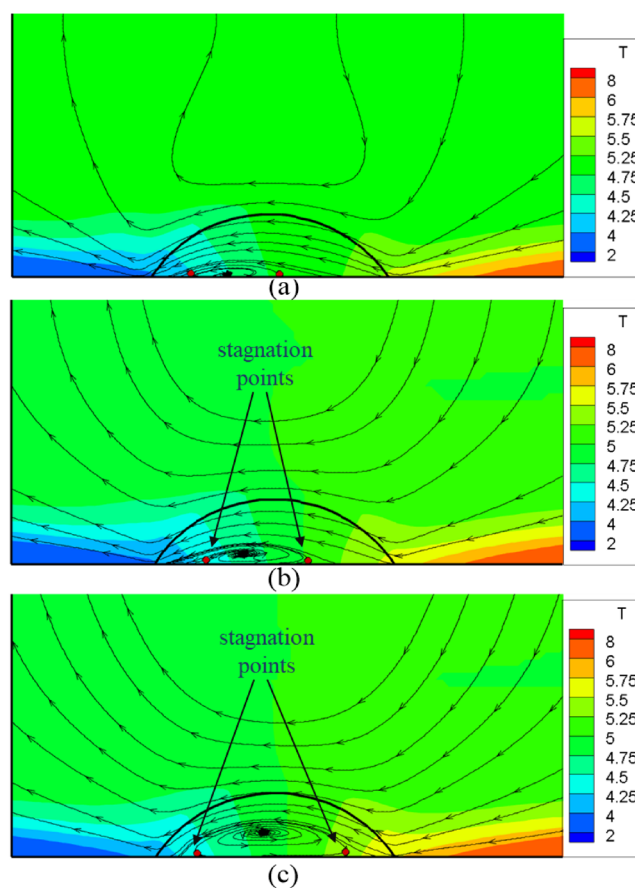

Figure 9. Steady flow patterns and temperature fields on the $x-z$ meridian surface of droplet at contact angle $\theta = 60°$ at viscosity ratio (a) $R_v = 0.01$, (b) $R_v = 0.1$, and (c) $R_v = 1$.
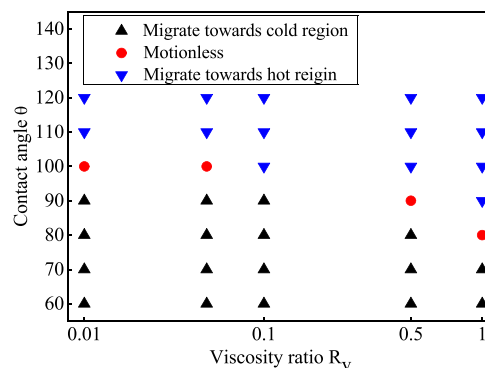

Figure 10. Phase diagram of the droplet migration direction under different contact angles and viscosity ratios.

attributed to the higher Prandtl number that can enhance convective heat transfer; thereby, the temperature gradient along the droplet surface is reduced as well as the thermocapillary flow. At contact angle $\theta = 60°$, both mechanical force and thermocapillary force drive the droplet toward the cold region. Weak thermocapillary flows result in a reduced driving force, leading to the decreasing migration speed. At $\theta = 120°$, the mechanical force drives the droplet toward the hot region while the thermocapillary flow contributes to migration toward the cold region; hence, weak thermocapillary flows result in increasing migration speed toward the hot region.
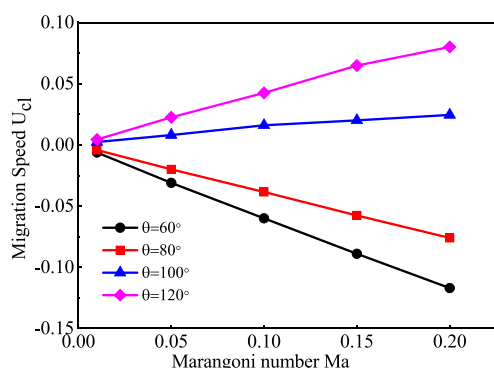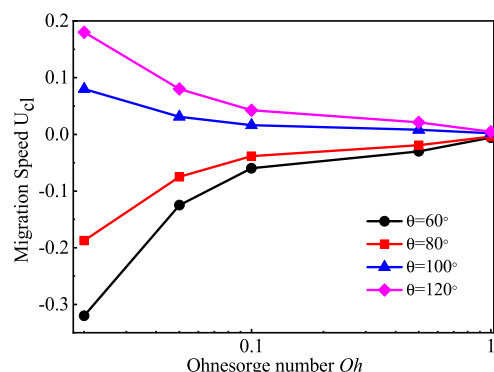
Figure 11. Effect of the Marangoni number on the droplet migration speed under different contact angles.
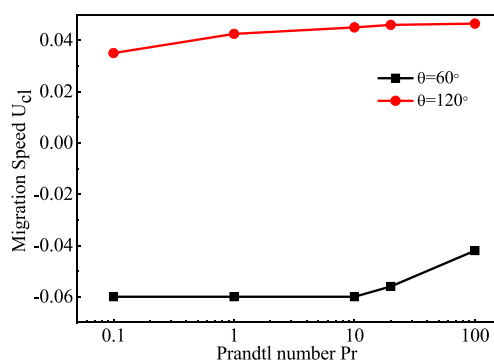
Figure 12. Effect of the Prandtl number on the droplet migration speed under different contact angles.

Figure 13 shows the effect of the Ohnesorge number on the migration speed under different contact angles. As the

Figure 13. Effect of the Ohnesorge number on droplet migration speed under different contact angles.

Ohnesorge number increases, the viscous shear force is increased. Although the mechanical force remains unchanged, the overall driving force is reduced, resulting in a decrease in droplet migration speed.

5. CONCLUSIONS

The migration of the sessile droplet can be controlled through a thermocapillary force. In the study, a three-dimensional model with the level-set method is established to numerically simulate the migration of a sessile droplet on a substrate with constant temperature gradient. The moving contact lines are implemented by the line-to-plane construction method with the

Navier slip boundary condition. After the model is validated with reliable theoretical results, the droplet migration speed and direction are studied under different contact angles, dynamic viscosity ratios, Marangoni numbers, Ohnesorge numbers, and Prandtl numbers. The main findings are as follows:

1. With the increasing contact angle, the droplet first migrates toward the cold region of the substrate, and the migration speed increases under $\theta \leq 60°$ while it decreases at $60° \leq \theta \leq 90°$. Then, the droplet migrates toward the hot region and speed increases at $\theta \geq 100°$.

2. The large viscosity ratio of surrounding gas over the liquid droplet can decrease the droplet migration speed due to enhanced viscous force surrounding the droplet. Furthermore, it can also cause the migration direction to transit from toward the cold region to toward the hot region.

3. The droplet migration speed is increased by the enhanced thermocapillary force with the increasing Marangoni number, and it is decreased by increasing the Ohnesorge number due to the increased viscous force. Neither of the two numbers can change the migration direction of the droplets.

4. Increasing the Prandtl number results in reduction of the temperature difference within the droplet, as well as the thermocapillary flows. This can lead to the increasing migration speed of the droplet toward the hot region, while decreasing migration speed toward the cold region.

■ AUTHOR INFORMATION

Corresponding Authors

Yong-Pan Cheng − *Beijing Key Laboratory of Multiphase Flow and Heat Transfer for Low Grade Energy, North China Electric Power University, Beijing 102206, China;* orcid.org/0000-0001-6955-4296; Email: chengyp@ncepu.edu.cn

Wei-Cheng Yan − *School of Chemistry and Chemical Engineering, Jiangsu University, Zhenjiang, Jiangsu 212013, China;* orcid.org/0000-0002-6820-8815; Email: yanwc@ujs.edu.cn

Authors

Jin-Xin Wang − *Beijing Key Laboratory of Multiphase Flow and Heat Transfer for Low Grade Energy, North China Electric Power University, Beijing 102206, China*

Fei-Yu Zhang − *Beijing Key Laboratory of Multiphase Flow and Heat Transfer for Low Grade Energy, North China Electric Power University, Beijing 102206, China*

Shi-Yu Li − *Beijing Key Laboratory of Multiphase Flow and Heat Transfer for Low Grade Energy, North China Electric Power University, Beijing 102206, China*

Fan Wang − *School of Quality and Technical Supervision, Hebei University, Baoding, Hebei 071002, China*

Jin-Liang Xu − *Beijing Key Laboratory of Multiphase Flow and Heat Transfer for Low Grade Energy, North China Electric Power University, Beijing 102206, China;* orcid.org/0000-0003-0145-9983

Yi Sui − *School of Engineering and Materials Science, Queen Mary University of London, London E1 4NS, United Kingdom*

Complete contact information is available at:
https://pubs.acs.org/10.1021/acs.iecr.3c02809

REFERENCES

(1) Zhang, W. W.; Li, Y. Y.; Long, W. J.; Cheng, W. L. Enhancement Mechanism of High Alcohol Surfactant on Spray Cooling: Experimental Study. *Int. J. Heat Mass Trans.* **2018**, *126*, 363−376.

(2) Wang, J.; Dong, T.; Cheng, Y.; Yan, W. C. Machine Learning Assisted Spraying Pattern Recognition for Electrohydrodynamic Atomization System. *Ind. Eng. Chem. Res.* **2022**, *61* (24), 8495−8503.

(3) Chen, P.; Ouyang, F.; Wang, G.; Qi, H.; Xu, W.; Yang, W.; Zhang, Y.; Lan, Y. Droplet Distributions in Cotton Harvest Aid Applications Vary with the Interactions Among the Unmanned Aerial Vehicle Spraying Parameters. *Ind. Crops Prod.* **2021**, *163*, No. 113324.

(4) Gelin, P.; Bihi, I.; Ziemecka, I.; Thienpont, B.; Christiaens, J.; Hellemans, K.; Maes, D.; De Malsche, W. Microfluidic Device for High-Throughput Production of Monodisperse Droplets. *Ind. Eng. Chem. Res.* **2020**, *59* (28), 12784−12791.

(5) Jia, J.; Liu, R. K.; Gu, Y. H.; Sun, Q.; Wang, J. X.; Chen, J. F. High-gravity-assisted Fabrication of Self-assembled Colloidosomes. *Ind. Eng. Chem. Res.* **2022**, *61* (20), 6934−6944.

(6) Liu, J.; Yap, Y. F.; Nguyen, N. T. Numerical Study of the Formation Process of Ferrofluid Droplets. *Phys. Fluids* **2011**, *23* (7), No. 072008.

(7) Dong, T.; Wang, J. X.; Wang, Y.; Tang, G. H.; Cheng, Y. P.; Yan, W. C. Development of Machine Learning Based Droplet Diameter Prediction Model for Electrohydrodynamic Atomization Systems. *Chem. Eng. Sci.* **2023**, *268*, No. 118398.

(8) Dai, Q.; Huang, W.; Wang, X. Contact Angle Hysteresis Effect on the thermocapillary Migration of Liquid Droplets. *J. Colloid Interface Sci.* **2018**, *515*, 32−38.

(9) Ma, Y.; Cheng, Y.; Shen, Y.; Xu, J.; Sui, Y. Manipulation of Bubble Migration Through Thermal Capillary Effect under Variable Buoyancy. *Int. J. Therm. Sci.* **2020**, *149*, No. 106199.

(10) Karapetsas, G.; Chamakos, N. T.; Papathanasiou, A. G. thermocapillary Droplet Actuation: Effect of Solid Structure and Wettability. *Langmuir* **2017**, *33* (41), 10838−10850.

(11) Bjelobrk, N.; Girard, H. L.; Bengaluru Subramanyam, S.; Kwon, H. M.; Quéré, D.; Varanasi, K. K. thermocapillary Motion on Lubricant-Impregnated Surfaces. *Phys. Rev. Fluids* **2016**, *1* (6), No. 063902.

(12) Shen, Y.; Kang, F.; Cheng, Y. P.; Zhang, K.; Sui, Y. Numerical and Theoretical Analysis of Fast Evaporating Sessile Droplets with Coupled Fields. *Int. J. Therm. Sci.* **2022**, *172*, No. 107284.

(13) Kang, F.; Shen, Y.; Cheng, Y.; Li, N. Lifetime Prediction of Sessile Droplet Evaporation with Coupled Fields. *Ind. Eng. Chem. Res.* **2021**, *60* (43), 15782−15792.

(14) Chaudhury, M. K.; Chakrabarti, A.; Daniel, S. Generation of Motion of Drops with Interfacial Contact. *Langmuir* **2015**, *31* (34), 9266−9281.

(15) Bouasse, H. *Capillarité: Phénomènes Superficiels*; Delagrave: Paris France. 1924.

(16) Grutzmacher, P. G.; Jalikop, S. V.; Gachot, C.; Rosenkranz, A. thermocapillary Lubricant Migration on Textured Surfaces-a Review of Theoretical and Experimental Insights. *Surf. Topogr.: Metrol. Prop.* **2021**, *9* (1), No. 013001.

(17) Ford, M. L.; Nadim, A. thermocapillary Migration of an Attached Drop on a Solid Surface. *Phys. Fluids* **1994**, *6* (9), 3183−3185.

(18) Brochard, F. Motions of Droplets on Solid Surfaces Induced by Chemical or Thermal Gradients. *Langmuir* **1989**, *5* (2), 432−438.

(19) Dai, Q.; Khonsari, M. M.; Shen, C.; Huang, W.; Wang, X. On the Migration of a Droplet on an Incline. *J. Colloid Interface Sci.* **2017**, *494*, 8−14.

(20) Masoud, H.; Stone, H. A. The Reciprocal Theorem in Fluid Dynamics and Transport Phenomena. *J. Fluids Mech.* **2019**, *879*, P1.

(21) Sui, Y. Moving Towards the Cold Region or the Hot Region? thermocapillary Migration of a Droplet Attached on a Horizontal Substrate. *Phys. Fluids* **2014**, *26* (9), No. 092102.

(22) Wasan, D. T.; Nikolov, A. D.; Brenner, H. Droplets Speeding on Surfaces. *Science* **2001**, *291* (5504), 605−606.

(23) Pradhan, T. K.; Panigrahi, P. K. thermocapillary Convection inside a Stationary Sessile Water Droplet on a Horizontal Surface with an Imposed Temperature Gradient. *Exp. Fluids* **2015**, *56* (9), 178.

(24) Fath, A.; Bothe, D. Direct Numerical Simulations of thermocapillary Migration of a Droplet Attached to a Solid Wall. *Int. J. Multiphase Flow* **2015**, *77*, 209−221.

(25) Yin, Z.; Chang, L.; Hu, W.; Li, Q.; Wang, H. Numerical Simulations on thermocapillary Migrations of Nondeformable Droplets with Large Marangoni Numbers. *Phys. Fluids* **2012**, *24* (9), No. 092101.

(26) Nguyen, H. B.; Chen, J. C. A numerical Study of thermocapillary Migration of a Small Liquid Droplet on a Horizontal Solid Surface. *Phys. Fluids* **2011**, *23* (1), No. 019901.

(27) Balasubramaniam, R.; Subramanian, R. S. The Migration of a Drop in a Uniform Temperature Gradient at Large Marangoni Numbers. *Phys. Fluids* **2000**, *12* (4), 733−743.

(28) Zhao, Y. J.; Liu, F. J.; Chen, C. H. thermocapillary Actuation of Binary Drops on Solid Surfaces. *Appl. Phys. Lett.* **2011**, *99* (10), 104101.

(29) Tseng, Y. T.; Tseng, F. G.; Chen, Y. F.; Cheng, C. C. Fundamental Studies on Micro-droplet Movement by Marangoni and Capillary Effects. *Sens. Actuators A* **2004**, *114* (2−3), 292−301.

(30) Wu, Z. B. thermocapillary Migration of a Planar Droplet at Small and Large Marangoni Numbers: Effects of Interfacial Rheology. *Z. Angew. Math. Phys.* **2020**, *71* (1), 8.

(31) Xie, J. C.; Lin, H.; Zhang, P.; Liu, F.; Hu, W. R. Experimental Investigation on thermocapillary Drop Migration at Large Marangoni Number in Reduced Gravity. *J. Colloid Interface Sci.* **2005**, *285* (2), 737−743.

(32) Ma, Y.; Cheng, Y. P.; Shen, Y.; Xu, J. L.; Sui, Y. Manipulation of bubble migration through thermal capillary effect under variable buoyancy. *Int. J. Therm. Sci.* **2020**, *149*, No. 106199.

(33) Sui, Y.; Spelt, P. D. M. An Efficient Computational Model for Macroscale Simulations of Moving Contact Lines. *J. Comput. Phys.* **2013**, *242*, 37−52.

(34) Cheng, Y. P.; Wang, F.; Xu, J. L.; Liu, D.; Sui, Y. Numerical Investigation of Droplet Spreading and Heat Transfer on Hot Substrates. *Int. J. Heat Mass Trans.* **2018**, *121*, 402−411.

(35) Zhang, B.; Liu, D.; Cheng, Y. P.; Xu, J. L.; Sui, Y. Numerical Investigation on Spontaneous Droplet/Bubble Migration under Thermal Radiation. *Int. J. Therm. Sci.* **2018**, *129*, 115−123.

(36) Sui, Y.; Ding, H.; Spelt, P. D. M. Numerical Simulations of Flows with Moving Contact Lines. *Ann. Rev. Fluid Mech.* **2014**, *46*, 97−119.

(37) Sui, Y.; Spelt, P. D. M. Validation and Modification of Asymptotic Analysis of Slow and Rapid Droplet Spreading by Numerical Simulation. *J. Fluid Mech.* **2013**, *715*, 283−313.

(38) Spelt, P. D. M. A Level-Set Approach for Simulations of Flows with Multiple Moving Contact Lines with Hysteresis. *J. Comput. Phys.* **2005**, *207* (2), 389−404.

(39) Russo, G.; Smereka, P. A Remark on Computing Distance Functions. *J. Comput. Phys.* **2000**, *163* (1), 51−67.